



Label-free electrochemical biosensor for determination of procalcitonin based on graphene-wrapped Co nanoparticles encapsulated in carbon nanobrushes coupled with AuPtCu nanodendrites

Xin-Yue Ge¹ · Jing-Xian Zhang¹ · Yi-Ge Feng¹ · Ai-Jun Wang¹ · Li-Ping Mei¹ · Jiu-Ju Feng¹

Received: 28 November 2021 / Accepted: 6 January 2022 / Published online: 17 February 2022
© The Author(s), under exclusive licence to Springer-Verlag GmbH Austria, part of Springer Nature 2022

Abstract

A new label-free electrochemical immunosensor was constructed for quantitative detection of procalcitonin (PCT), by employing AuPtCu nanodendrites (AuPtCu NDs, prepared by a one-pot solvothermal method) and graphene-wrapped Co nanoparticles encapsulated in 3D N-doped carbon nanobrushes (G-Co@NCNBs), obtained by self-catalyzed chemical vapor deposition as immune-sensing platform. Impressively, the home-made nanocomposite enlarged the highly accessible active sites and promoted the mass/electron transport, in turn showing the efficient synergistic catalysis towards H₂O₂ reduction, combined by greatly increasing the loading capacity of the PCT antibody (Ab). The as-constructed sensor displayed a dynamic linear range of 0.0001 ~ 100 ng mL⁻¹ along with an ultra-low limit of detection (LOD = 0.011 pg mL⁻¹, S/N = 3) and was further explored for determination of PCT in a diluted serum sample with acceptable results. The sensor provides some valuable guidelines for bioassay and early diagnosis of sepsis.

Keywords Label-free immunosensor · Nanobrushes · Nanodendrites · Synergistic signal magnification · Procalcitonin

Introduction

Septicemia remains a major public healthcare problem affecting significant morbidity and mortality [1], which is mainly triggered by pathogenic agents such as fungi, microbes, viruses, and parasites [2]. In general, septicemia causes systemic embolization and metastatic infections, further inducing the mortality of up to 66% of patients [3]. Consequently, it is extremely significant for early and sensitive diagnosis of septicemia.

For determination of septicemia, C-reactive protein (CRP), cytokines, and procalcitonin (PCT, a precursor of the hormone calcitonin) commonly work as important biomarkers [2]. Among them, PCT is particularly recognized as a principal and reliable biomarker in clinical diagnosis

of sepsis, which is mainly secreted by C cells of the thyroid as well as the intestine and neuroendocrine cells of the lung [4–6]. Under normal physiological conditions, the PCT level is below 0.25 ng mL⁻¹, while its threshold value is instantly elevated at the beginning of a serious inflammatory response [5, 7]. It emphasizes the importance of quantification of PCT in early detection of septicemia, as far as the reduced risk of infection and mortality.

For quantitative immunoassay of PCT so far, many immuno-methods have been developed, including chemiluminescence (CL) [8], colorimetry [9], fluorescence [4], and electrochemistry [10]. Among them, electrochemical immunosensors display rapid development due to their arresting characteristics (e.g., simple operation, fast response, and cost-effectiveness) [11]. Notably, label-free immunosensors hold great promise for practical analysis of PCT [12, 13], thanks to their simplicity and easy fabrication, as well as the less chemicals used than the sandwich-typed counterparts [14].

Typically, how to transform certain bio-recognition event into readable electrical signals plays a key role in the immune-sensing system [14]. For signal magnification, diverse nanomaterials especially noble metal (e.g., Au, Pt,

✉ Jiu-Ju Feng
jjfeng@zjnu.cn

¹ Key Laboratory of the Ministry of Education for Advanced Catalysis Materials, College of Chemistry and Life Sciences, College of Geography and Environmental Sciences, Zhejiang Normal University, Jinhua 321004, China

and Ag) materials have wide applications in biosensing field, owing to their intrinsic advantages such as large surface area, superior biocompatibility, and good electrical conductivity [15, 16]. Particularly, Au@Pt nanocrystals were employed for specific recognition and ultrasensitive assay of prostate-specific antigen in label-free sensors [15, 16].

However, the widespread use of noble metal inevitably suffers from the high cost and resource scarcity, which severely restricts the further development [17, 18]. Given this, much research is focused on incorporation of transition metals (e.g., Cu and Co) in precious metal-alloyed nanomaterials as reliable substitutes for their good chemical stability, high electronic conductivity, and catalytic activity [13, 18]. As lately reported, Pd nanoparticles (NPs) modified MoS₂/NiCo heterostructures were employed to establish the immunosensor for sensitive analysis of procalcitonin, which displayed excellent electrocatalytic ability towards H₂O₂ reduction [12].

Apart from the compositions, metal nanostructures and shapes also have close association with the surface and catalytic properties [19]. For building the above sensors, there recently emerge diverse shapes of nanomaterials such as wires [17], hollow frames [20], and dendrites [21]. Among them, dendritic nanostructures (e.g., Au@Pd nanodendrites [22], and AgPtCo nanodendrites [23]) exhibit the large surface areas and abundant tunable pores, which can load more biomolecules and facilitate the electron transfer [12], finally harvesting the superior analytical performance.

To date, an ever-increasing number of three-dimensional hierarchical multi-scaled carbon nanomaterials such as carbon nanotubes (CNTs) [14] and graphene oxide [24] are employed as feasible supporting matrix for construction of the immunosensors, due to their outstanding electronic conductivity, large surface area, and good biocompatibility [14, 25, 26]. As early reported, carbon brush-like architectures show superior electrocatalytic activity to the CNTs in high-efficiency rechargeable Zn-air batteries [27], mainly attributing to the structural advantage and synergic effects among carbon and metal compositions, along with the promoted electron transfer kinetics between diverse electroactive substances [24].

Herein, AuPtCu nanodendrites (AuPtCu NDs) and graphene-wrapped Co NPs encapsulated in 3D N-doped carbon nanobrushes (G-Co@NCNBs) were synthesized via a facile one-pot solvothermal strategy and self-catalyzed chemical vapor deposition, respectively. By uniformly blending them together, the catalytic property of the resulting nanocomposite was critically investigated, coupled by illustrating their catalytic mechanism in some detail. Then, a label-free electrochemical immunosensor was prepared for bioassay of PCT via signal amplification for H₂O₂ reduction, which subsequently extended its application in diluted serum samples.

Experimental section

Preparation of G-Co@NCNBs

Typically, the G-Co@NCNBs were synthesized according to the previous research by replacing melamine with dicyandiamide [27]. In short, 42.8 mg of CoCl₂ was first dissolved into 30 mL of water. Then, 17.2 mg of nitrilotriacetic acid and 10.0 mL of isopropyl alcohol were separately dropped into the above-mixed solution and transferred into a Teflon-lined stainless-steel autoclave (180 °C, 6 h) to form Co-oxo framework nanowires. Subsequently, 50 mg of the above prepared wire-like precursor and 2 g of dicyandiamide were put into two separate ceramic boats with the precursor at the downstream side in a tube furnace, accompanied by gradually heating from room temperature (25 °C) to 700 °C at a rate of 6 °C min⁻¹ in N₂ atmosphere with the pyrolysis time of 2 h. After cooling down naturally, the resulting black sample was collected, termed as G-Co@NCNBs for simplicity.

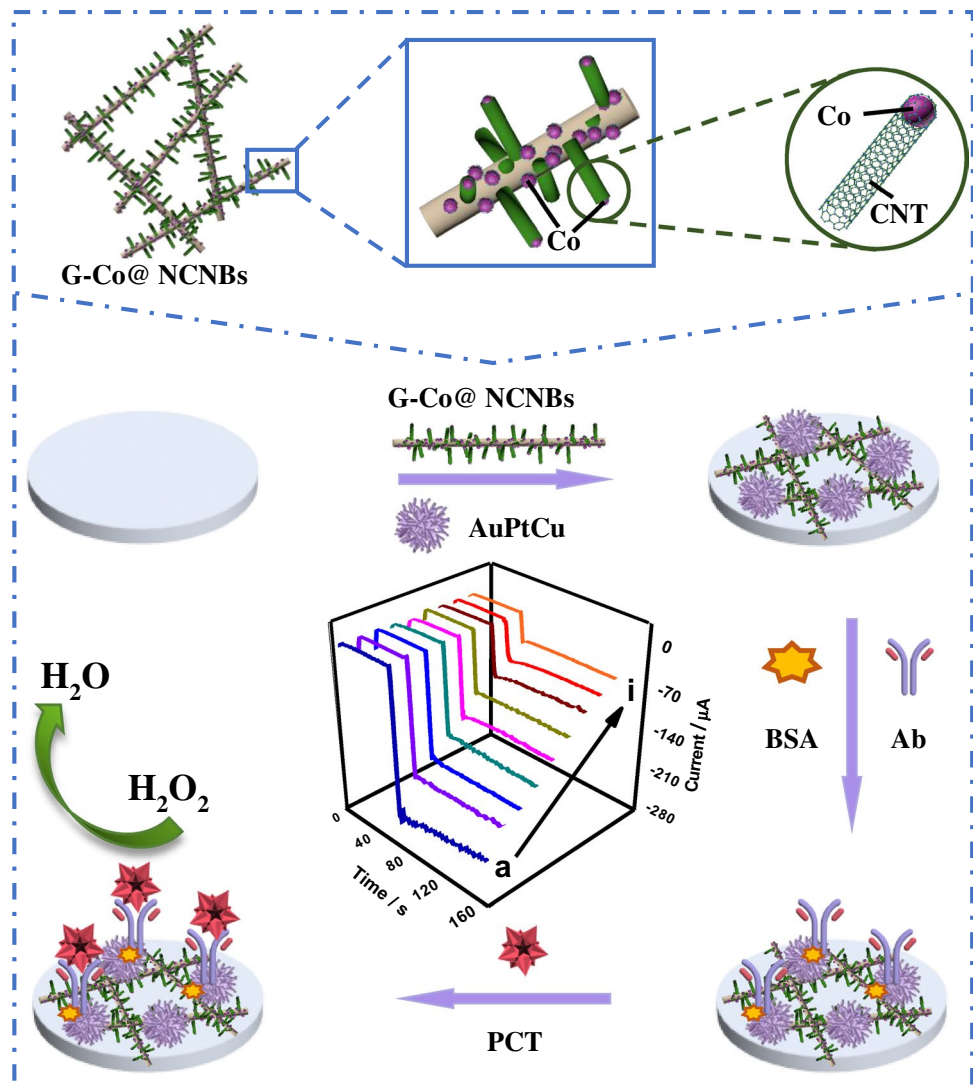
Preparation of AuPtCu NDs

The AuPtCu NDs were synthesized by an eco-friendly one-pot solvothermal method. Typically, 160.00 mg of CTAC was dissolved into 20.0 mL of oleylamine (OAm). After the complete dissolution, 1.65 mL of HAuCl₄ (24.3 mmol L⁻¹), 15.7 mg of Pt(acac)₂, and 10.5 mg of Cu(acac)₂ were successively dispersed into the above mixture. Next, 183.9 mg of ciprofloxacin hydrochloride monohydrate was put into the reaction system under stirring and ultrasonicated to obtain a homogeneous suspension. Finally, the suspension was decanted into a Teflon-lined stainless autoclave and heated at 180 °C for 10 h. After cooling down in air, the resultant product was completely washed with ethanol and water, followed by drying in a vacuum at 60 °C before use.

Preparation of the label-free immunosensor

Figure 1 exhibits the stepwise construction of the immunosensor. In this work, the AuPtCu NDs (1.0 mg) and G-Co@NCNBs (1.0 mg) were dissolved in 1.0 mL of a mixed solution of water and ethanol with an equal volume under ultrasonication to form a homogeneous suspension (2.0 mg mL⁻¹). Then, 2 μL of the AuPtCu NDs/G-Co@NCNBs suspension was first dropped on the freshly cleaned glassy carbon electrode (GCE, 3 mm in diameter) and dried in air. After that, 6 μL of the PCT antibody (Ab) solution (10 μg mL⁻¹) was immobilized on the modified electrode and dried at 4 °C overnight [18, 28], followed by casting 5 μL of the bovine serum albumin (BSA) solution (1.0

Fig. 1 Schematic illustration of the AuPtCu NDs/G-Co@NCNBs-based immunosensor for detecting PCT



wt%) to cover the nonspecific binding sites with the amine groups [29] and keeping at 37 °C for 30 min. Finally, the above electrode was immersed into the PCT solutions in the scope of 0.0001 ~ 100 ng mL⁻¹ at 37 °C for 50 min to ensure the specific immunological recognition. Notably, the coated electrode was thoroughly rinsed with phosphate-buffered solution (PBS, 0.1 mol L⁻¹, pH 7.4) after each step to remove unbounded substances, and the resultant immunosensor was stored at 4 °C prior to use.

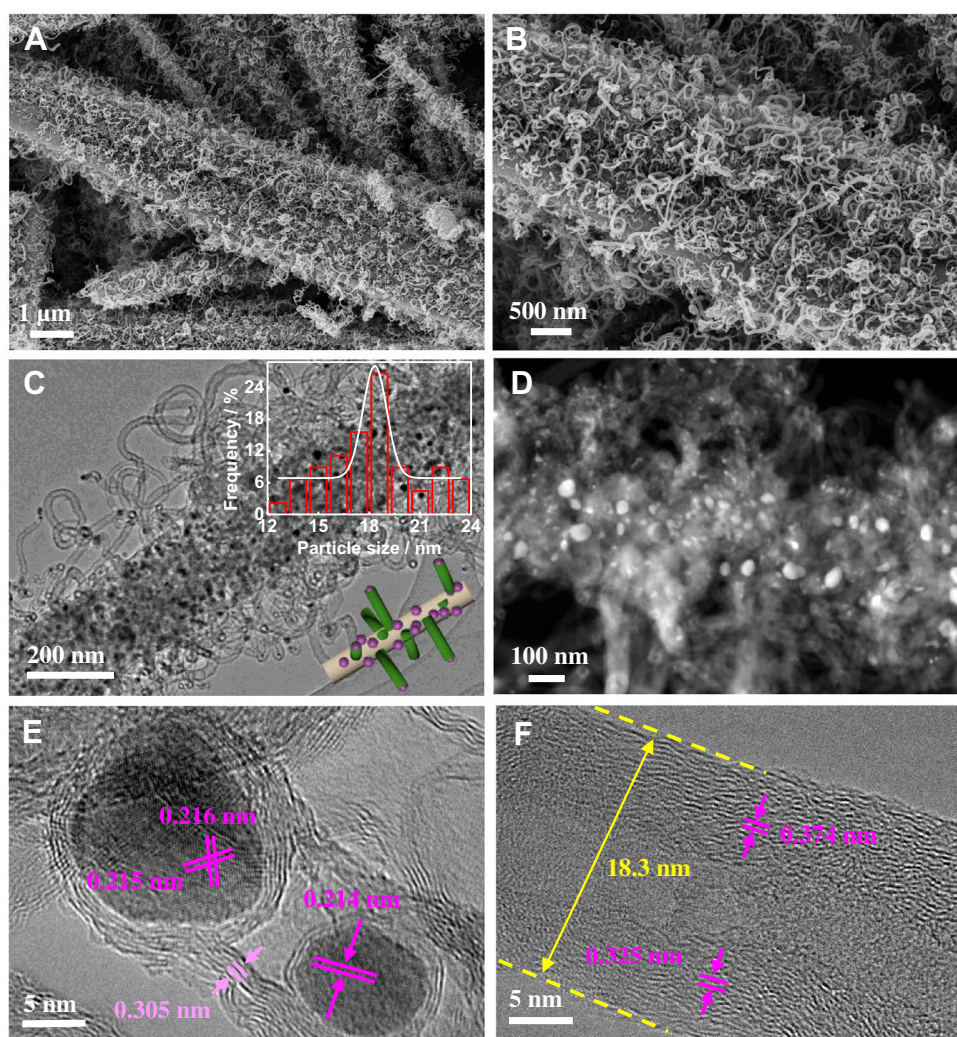
More detailed illustrations about the chemicals, apparatus, and electrochemical measurements were provided in the [Supporting Information \(SI\)](#).

Results and discussion

Characterizations of the G-Co@NCNBs

The morphology and structure of the G-Co@NCNBs were critically characterized by scanning electron microscopy (SEM). As displayed in the SEM image (Fig. 2A–B), the sample exhibits uniformly brush-like morphology with interconnected structure, as further confirmed by the transmission electron microscopy (TEM) image (Fig. 2C). Briefly, there are a large number of ultra-long thin tube-like branches entrapped in the entire fiber-like structure [27]. The high-angle annular dark field-scanning transmission electron microscopy (HAADF-STEM) image (Fig. 2D) clearly illustrates the Co NPs entrapped in the carbon nanobrushes with a diameter range of 13 ~ 24 nm

Fig. 2 (A–B) SEM images of the G-Co@NCNBs. The (C) low- and (E–F) high-resolution TEM images. The (D) HAADF-STEM images. Insets in (C) display the particle-size histogram of Co and 3D geometric model, respectively



and a mean diameter of 18.13 nm, as depicted by the particle-size histogram (inset in Fig. 2C). The high-resolution TEM (HR-TEM) images (Fig. 2E–F) reveal the interplanar spacing distance of 0.305 nm (Fig. 2E), 0.325 nm and 0.375 nm (Fig. 2F) in the gray lattice fringes corresponding to graphitic carbon, while those of 0.214 nm, 0.215 nm, and 0.216 nm (Fig. 2E, marked from the dark nanoclusters) correlate to the (100) planes of Co [30], reflecting efficient encapsulation of the Co particle by a thin layer of graphitic carbon. Additionally, the tube-like graphitic carbon with an approximately diameter of 18.3 nm clearly shows up in the HR-TEM image (Fig. 2F).

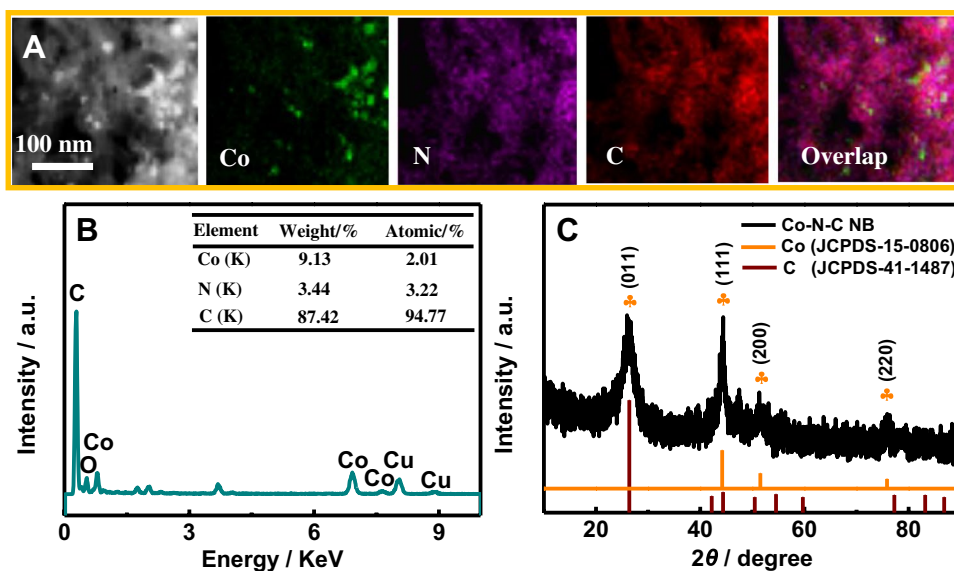
Figure 3A displays the high-angle annular dark field-scanning transmission electron microscopy energy-dispersive X-ray spectroscopy (HAADF-STEM-EDS) mappings. Plainly, the signals of Co show up at the border of the brush-like structure according to the overlap image, while N and C elements exhibit the homogenous distributions over the whole configurations, in good accordance with the energy-dispersive X-ray spectroscopy (EDS) analysis

where the atomic Co/N/C ratio is 2.01: 3.22: 94.77 in the sample (Fig. 3B).

X-ray diffraction (XRD) analysis was conducted to have more insights into the structure [31, 32]. As Fig. 3C describes, the three diffraction peaks at 44.35°, 51.81°, and 75.99° are well indexed to the (111), (200), and (220) planes of standard cubic Co (JCPDS-15-0806) [27], respectively. Besides, the peak at 26.39° corresponds to the (011) planes of bulk carbon (JCPDS-41-1487). These results reflect the successful synthesis of the G-Co@NCNBs.

The surface property of the G-Co@NCNBs was further investigated by X-ray photoelectron spectroscopy (XPS) analysis (Fig. S1A, SI). The survey XPS spectrum demonstrates the co-presence of Co, O, N, and C elements, which agrees well with the EDS analysis. As observed in Fig. S1B (SI), the binding energies of the Co 2p_{1/2} and Co 2p_{3/2} peaks at 796.31 eV and 780.63 eV refer to metallic Co⁰ species [33]. Besides, the weaker ones at 803.40 eV and 786.31 eV come from Co 2p_{1/2} and Co 2p_{3/2} of CoO, due to the unavoidable oxidation upon exposure to the aerobic atmosphere.

Fig. 3 (A) HAADF-STEM-EDS mappings, (B) EDS spectrum, and (C) XRD pattern of G-Co@NCNBs. Inset in (B) shows the weight and atomic ratios of Co, N, and C



The five main peaks at 398.49 eV, 399.11 eV, 401.03 eV, 401.82 eV, and 405.03 eV in the N 1s XPS segment (Fig. S1C, SI) correlate to pyridinic-N, Co-N_x, pyrrolic-N, graphitic N, and oxidized-N [34]. Importantly, the pyridinic N would create more active sites, which are beneficial to the catalytic activity [33]. The XPS spectra further identify different N states existed in the graphitic carbon [35]. Also, the C 1s section (Fig. S1D, SI) reveals the peaks at 284.82 eV, 285.71 eV, and 289.15 eV associated with the C–C, C=N, and C=O groups, respectively. More importantly, the present C=N further certifies the formation of the N-doped carbon skeleton [36], obviously showing the efficient doping of nitrogen into the graphitic structure.

The D and G bands located at 1370.23 and 1594.98 cm⁻¹ (Fig. S1, SI) relate to the graphitic defects and sp²-hybridized graphitic carbon in the Raman spectrum of the carbon-derived materials [30], respectively. Their intensity ratio (I_D/I_G) is found to be roughly 1.002, suggesting the high degree of graphitization in the G-Co@NCNBs that would enhance the electronic conductivity [37, 38].

Characterizations of AuPtCu NDs

TEM was adopted to investigate the morphology of advanced nanomaterials [12, 39]. As seen in Fig. 4A–B, there emerge several uniformly dispersed particles with dendritic structures in the medium-resolution TEM images. According to the particle-size histogram (inset in Fig. 4A), the particle sizes roughly emerge from 44 to 56 nm with an average diameter of 49.61 nm.

Such hierarchical architecture can be further examined by the high-resolution TEM image (Fig. 4C). The lattice spacing distances in the well-resolved fringes are measured to be approximately 0.215 nm and 0.217 nm, because of

the constraint of the (111) facets of the face-centered cubic (fcc) AuPtCu alloy [40]. Their polycrystalline property is well certified by the corresponding selected area electron diffraction (SEAD) pattern (inset in Fig. 4B) [41].

XRD analysis was adopted to characterize the crystal phase [37]. As depicted in Fig. 4D, four obvious diffraction peaks at 38.75°, 44.57°, 65.07°, and 78.64° are in good line with the (111), (200), (220), and (311) facets of the face-centered cubic (fcc) AuPtCu alloy [40]. It is noted that these peaks appear between those of bulk Au (JCPDS-04-0784), Pt (JCPDS-04-0836), and Cu (JCPDS-04-0802). Additionally, there hardly finds any single-component peak of pure Au, Pt, or Cu in the XRD analysis, suggesting the single-phased alloy formed in the AuPtCu NDs [42, 43].

Figure 5A displays the HAADF-STEM-EDS elemental mappings, exhibiting the relatively homogeneous distributions of Au, Pt, and Cu elements across the whole particles [44], certifying the alloy feature again, as further evidenced by the elemental line-scanning profiles (Fig. 5B). The atomic ratio of the Au/Pt/Cu is roughly 1.26: 92.57: 6.17 in this sample based on the EDS elemental analysis (Fig. 5C) [31].

XPS was adopted to further understand the metal compositions and valence states of the AuPtCu NDs [44]. The full-scan spectrum shows the homogeneous presence of Au, Pt, Cu, and C elements in the product (Fig. S3A, SI), in good agreement with the EDS analysis. Further, the two characteristic peaks at 87.03 eV and 83.38 eV in the Au 4f section (Fig. S3B, SI) stem from Au⁰ 4f_{5/2} and Au⁰ 4f_{7/2}, while the weaker ones at 87.89 eV and 84.02 eV originate from Au⁺ 4f_{5/2} and Au⁺ 4f_{7/2} species, respectively. These observations match well with the standard XPS data of Au [45].

As seen in Fig. S3C (SI), the binding energies at 73.71 eV and 70.31 eV are well conformed with metallic Pt⁰ in the Pt 4f region with a spin-orbit splitting of 3.4 eV, which are

Fig. 4 (A–B) Medium- and (C) high-resolution TEM images of the AuPtCu NDs. (D) XRD pattern of the AuPtCu NDs. Insets in (A) and (B) exhibit the particle-size histogram and SEAD pattern, respectively

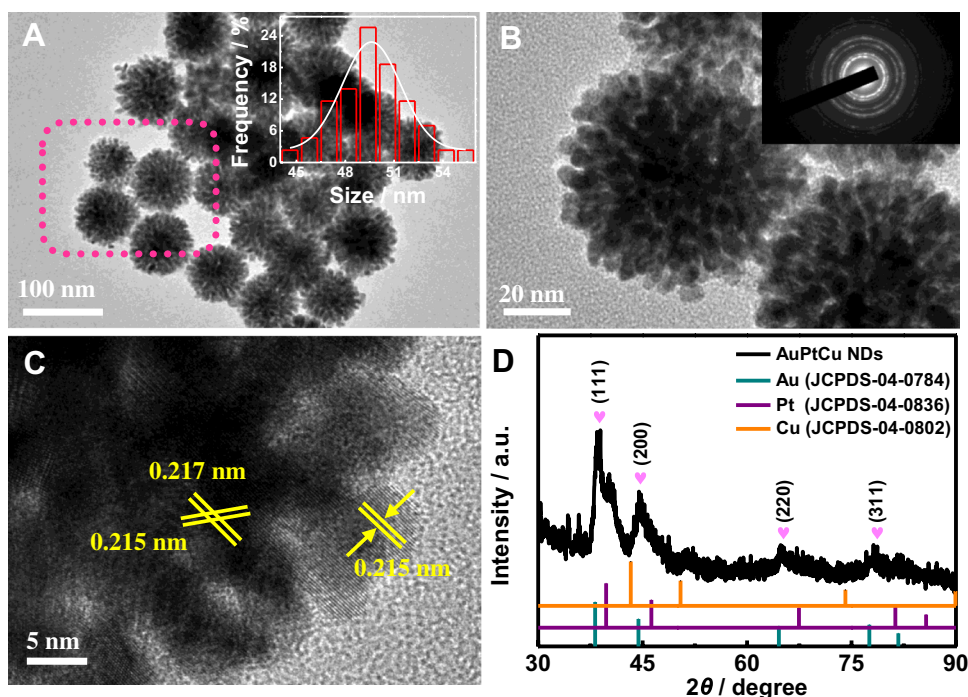
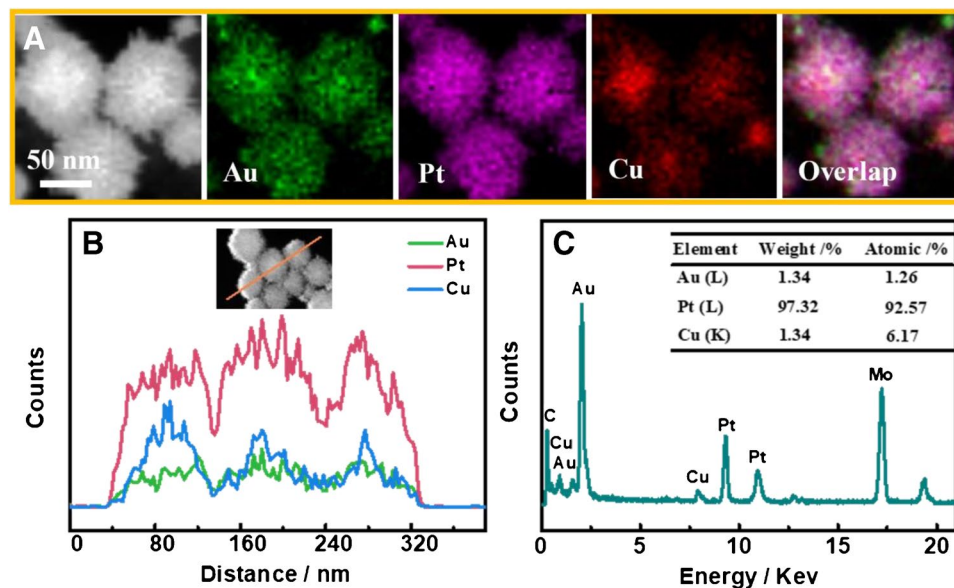


Fig. 5 (A) HAADF-STEM-EDS mappings, (B) line scanning profiles, and (C) EDS spectrum of the AuPtCu NDs. Insets in (B) and (C) show the HAADF-STEM image, and the weight and ratios of Au, Pt, and Cu, respectively



stronger than those of Pt^{2+} species at 75.41 eV and 71.54 eV, revealing the efficient reduction of the Pt precursor during the typical synthesis [17]. The slightly present Pt^{2+} species is ascribed to the inevitable oxidation of the sample in air [24]. The Pt 4f peaks located at the relatively higher binding energies than bulk Pt (70.61–71.30 eV for $4f_{7/2}$) further evidence the alloy feature with more electronegative Au [46].

Fig. S3D (SI) shows the Cu 2p segment, which can be separated into five sub-peaks. Specifically, there appear two prominent peaks at 951.00 eV and 931.32 eV, which are

assigned to $2p_{1/2}$ and $2p_{3/2}$ of Cu^0 , indicating the efficient reduction of the Cu salt [47]. Among the two Cu^0 peaks, the higher one located at 951.00 eV evidences the formation of the alloy with Au and Pt. The slight shift of the binding energy would modify the electronic structure and change the d-band center of Pt involved in the Fermi level [48]. Besides, the other two weaker ones at 953.43 eV and 934.88 eV are assigned to the Cu $2p_{1/2}$ and Cu $2p_{3/2}$ of Cu^{2+} species [49], coupled with a satellite peak at 943.26 eV associated with the Cu oxide. It means the high catalytic activity

of Cu atoms located on the alloy surface that can be easily oxidized, which would be instructive to the catalytic performance [47, 50].

As reported, the standard peaks of pure Au emerge at 84.0 eV for $4f_{7/2}$ and 87.7 eV for $4f_{5/2}$, those of Pt show up at 70.9 eV for $4f_{7/2}$ and 74.2 eV for $4f_{5/2}$, and those of Cu appear at approximately 931.9 eV for $2p_{3/2}$ and 951.8 eV for $2p_{1/2}$ [48]. By contrast with the above standard values, the binding energies of $Au^0 4f$ and $Cu^0 2p$ shift downward, while that of Pt^0 shows an upward shift. These scenarios demonstrate the electron transformation from Au and Cu to Pt, due to the more negative electronegativity of Pt [51].

According to the above discourses, the formation mechanism of the trimetallic AuPtCu NDs can be briefly described as follows: at the initial stage, the metal precursors (i.e., $H AuCl_4$, $Pt(acac)_2$, and $Cu(acac)_2$) are first reduced to Au, Pt, and Cu atoms by utilizing OAm as weak reductant [52]. As the reaction proceeds, the concentrations of the metal atoms gradually reach the supersaturation states, accompanied by forming AuPtCu nuclei through crystal fusion and assembly [53]. Eventually, the AuPtCu NDs are generated by anisotropic growth and Ostwald ripening under the guidance of CTAC and ciprofloxacin hydrochloride [54].

The electrochemical behaviors of AuPtCu NDs/G-Co@NCNBs

Chronoamperometry is an effective tool to extensively examine the electrocatalytic properties of advanced materials [17]. The catalytic properties of the AuPtCu NDs, G-Co@

NCNBs, and AuPtCu NDs/G-Co@NCNBs were critically investigated by acquiring the $i-t$ curves in the PBS (0.1 mol L^{-1} , pH 7.4) at -0.4 V upon addition of $5.0 \text{ mmol L}^{-1} H_2O_2$ after the background current reached steady (i.e., 60 s, Fig. 6A). The chronoamperometric current of the AuPtCu NDs/G-Co@NCNBs is larger than that of only AuPtCu NDs or G-Co@NCNBs under the identical conditions, on account of the synergetic effects of the AuPtCu NDs and G-Co@NCNBs [19]. Therefore, it is reliable to build a biosensor with the AuPtCu NDs/G-Co@NCNBs composite as the electrode material.

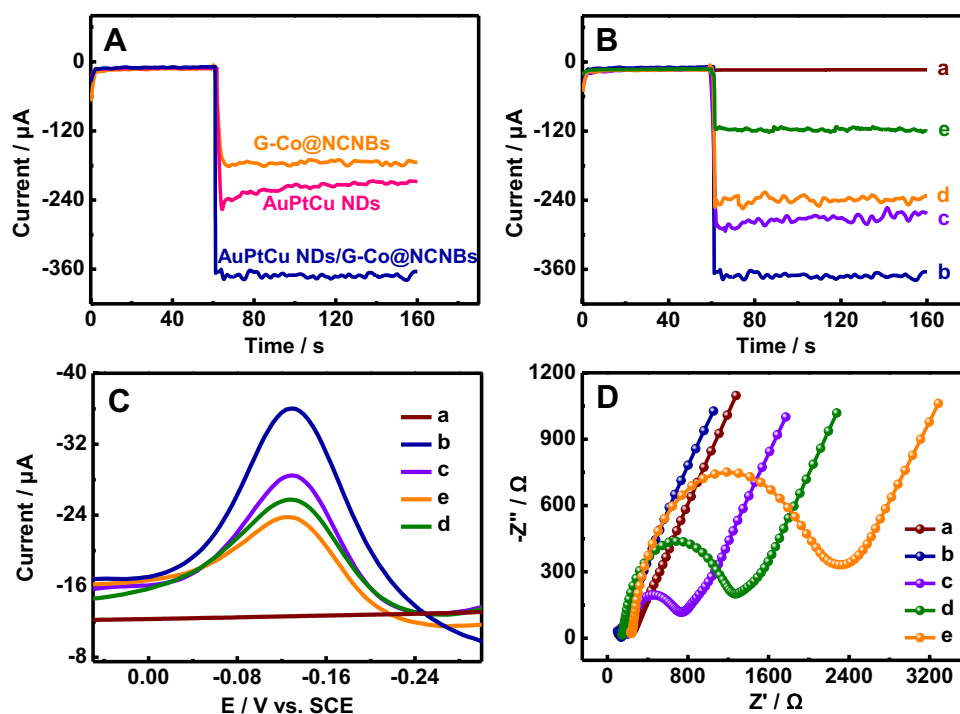
According to the previous research [10, 12], the electrocatalytic mechanism for H_2O_2 reduction at the AuPtCu NDs/G-Co@NCNBs can be described as follows:



Electrochemical characterizations of the immunosensor

The chronoamperometry test was conducted to monitor the stepwise construction of the AuPtCu NDs/G-Co@NCNBs-based immunosensor (Fig. 6B). Clearly, the AuPtCu NDs/G-Co@NCNBs/GCE shows the highly enlarged catalytic current upon addition of $5.0 \text{ mmol L}^{-1} H_2O_2$ (curve b) by

Fig. 6 (A) The $i-t$ curves of the investigated catalysts upon successive injection of $5.0 \text{ mmol L}^{-1} H_2O_2$ in 0.1 mol L^{-1} PBS (pH 7.4). The (B) $i-t$ curves and (C) DPV curves recorded during the stepwise construction of the immunosensor in the PBS at $5.0 \text{ mmol L}^{-1} H_2O_2$. (D) EIS plots acquired in 0.1 mol L^{-1} KCl solution containing $2.5 \text{ mmol L}^{-1} Fe(CN)_6^{3-/4-}$



contrast with bare GCE with nearly zero response (curve a), suggesting efficient immobilization of the AuPtCu NDs/G-Co@NCNBs. After successive incubation with the Ab (curve c), BSA (curve d), and PCT (curve e), the chronoamperometric signals gradually decline, owing to the severe blockage of interfacial electron transfer and difficult availability of the active sites covered by the immobilized bio-substances [19].

Differential pulse voltammetry (DPV) experiments were further carried out to monitor the step-wise construction at a sweep rate of 40 mV s^{-1} (Fig. 6C) [18]. In short, the peak current displays a distinct increase at the AuPtCu NDs/G-Co@NCNBs/GCE (curve b) over bare GCE (curve a). Next, the peak currents show a gradual downtrend by subsequently casting with the Ab (curve c) and BSA (curve d), confirming their successful immobilization in this research. Moreover, the detection signals continue to decay upon the modification of PCT, indicating the efficient immune-recognition event occurred in the sensing system. The above phenomena certificate successful fabrication of the biosensor for assay of PCT, also matching well with cyclic voltammetry analysis (CV, Fig. S4).

Apart from the above characterizations, electrochemical impedance spectroscopy (EIS) is also a powerful tool to further probe the interfacial changes during the step-by-step preparation of such a sensor [15]. Figure 6D shows the respective Nyquist plots recorded in the same surroundings as the above DPV and CV analysis. There is almost a straight line observed for the AuPtCu NDs/G-Co@NCNBs/GCE (curve b), reflecting the superior interfacial electron transport due to the superior electronic conductivity of the AuPtCu NDs/G-Co@NCNBs. Nonetheless, the electron transfer resistance (R_{et}) values are gradually enlarged by continuous incubation of Ab (curve c, $R_{\text{et}} = 738 \Omega$), BSA (curve d, $R_{\text{et}} = 1260 \Omega$), and PCT (curve e, $R_{\text{et}} = 2310 \Omega$), because the deposited immune complexes severely block the interfacial electron transport [41]. The above observations demonstrate feasibility of the as-built sensor for the follow-up PCT analysis.

Optimization of immunoassay parameters

To attain the largest catalytic signals for the bioanalysis of PCT, pH value of the buffer is a critical parameter in the analytical performance of the sensor, which exerts great influence on the catalytic reduction of H_2O_2 and bioactivity of the deposited bio-substances [11, 12]. As seen in Fig. 7A, the currents increase acutely in the range of 5.0–7.4 and then reach the maximum at pH 7.4, followed by an inverse decrease when the pH value is further extended up to 8.0. Thus, pH 7.4 was chosen to promote the catalysis and ready availability of the immune recognition.

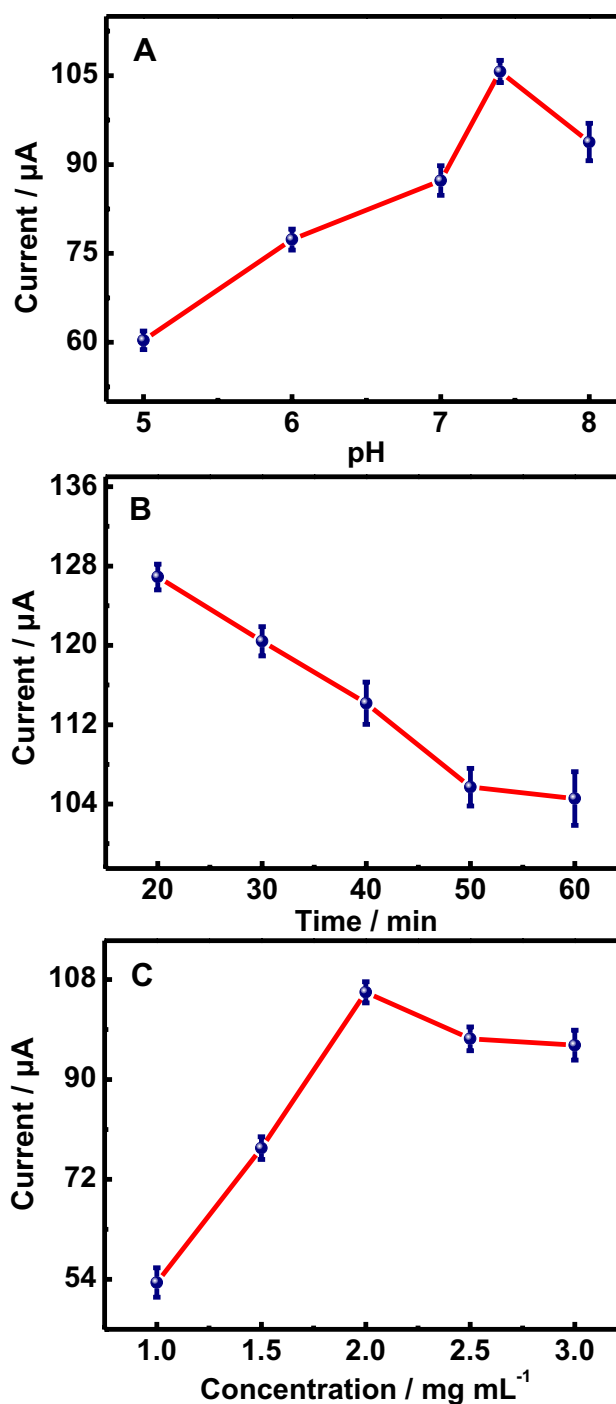


Fig. 7 The influences of the (A) pH, (B) incubation time, and (C) AuPtCu NDs/G-Co@NCNBs concentrations on the peak currents at 1.0 ng mL^{-1} PCT

It is well known that the incubation time is another major parameter that affects the immune-recognition [28]. As Fig. 7B depicts, the catalytic currents decay with the incubation time ranging from 20 to 50 min and then vary negligibly by further extending the time (e.g., 60 min), mainly owing to the completely saturated binding sites between the

Ab and PCT. Therefore, 50 min was adopted as the optimal time for this assay.

The concentration of the AuPtCu NDs/G-Co@ NCNBs suspension would have great effects on both the Ab loading and analytical performance [23]. As illustrated in Fig. 7C, the maximum response is acquired when the AuPtCu NDs/G-Co@ NCNBs concentration reaches 2.0 mg mL⁻¹ and then decreases slightly as the concentrations are further increased (e.g., 2.5 and 3.0 mg mL⁻¹), owing to serious inhibition of the interfacial electron transfer with the thickened film [18]. Hence, 2.0 mg mL⁻¹ of the AuPtCu NDs/G-Co@ NCNBs was chosen as the optimal concentration for the sequential analysis.

Analytical performance of the immunosensor

The quantitative determination of PCT was conducted by chronoamperometry on the label-free immunosensor based on the AuPtCu NDs/G-Co@ NCNBs (Fig. 8A). Shortly, the detection signals display gradual decay with an increase of the PCT concentrations up to 100 ng mL⁻¹ under the optimal conditions. The calibration plot (Fig. 8B) reveals proportional relationship between the current (*I*) and logarithm of the PCT concentration (log *C*_(PCT)) in a dynamic scope

of 0.0001–100 ng mL⁻¹, whose linear regression equation is described as $I = -25.19 \log C_{(PCT)} (\text{ng mL}^{-1}) + 105.19$ along with a correlation coefficient (R^2) of 0.9937 and a LOD of 0.011 pg mL⁻¹ ($S/N=3$). The slope of the calibration plot represents electrochemical sensitivity of the sensor with a value of 25.19 $\mu\text{A ng}^{-1} \text{mL}^{-1}$. The analytical performance of the as-established sensor is much comparable or even superior to previous PCT sensors by other analytical techniques in terms of the linear range and LOD such as sandwich imaging ellipsometry (the linear range: 0.125 ~ 128 ng mL⁻¹; LOD: 81 ng mL⁻¹) [55] and chemiluminescence using biotin streptavidin-mediated peroxidase nanocomplex (the linear range: 0.0025 ~ 80 ng mL⁻¹; LOD: 0.5 ng mL⁻¹) [8] (see details in Table 1). This comparison evidences the feasibility of the as-built sensor for highly sensitive assay of PCT.

Reproducibility, selectivity, and stability

Reproducibility is one of the pivotal characteristics of immunosensors [57]. To validate the reproducibility, five immunosensors were fabricated independently under equal conditions and measured by chronoamperometry

Fig. 8 (A) The *I*-*t* responses with different PCT concentrations: (curve a) 0 pg mL⁻¹, (curve b) 0.1 pg mL⁻¹, (curve c) 1.0 pg mL⁻¹, (curve d) 10.0 pg mL⁻¹, (curve e) 100.0 pg mL⁻¹, (curve f) 1.0 ng mL⁻¹, (curve g) 10.0 ng mL⁻¹, (curve h) 50.0 ng mL⁻¹, and (curve i) 100.0 ng mL⁻¹. (B) The calibration curve (Error bar = SD; *n* = 5). All of the tests were performed in the PBS containing 5.0 mmol L⁻¹ H₂O₂

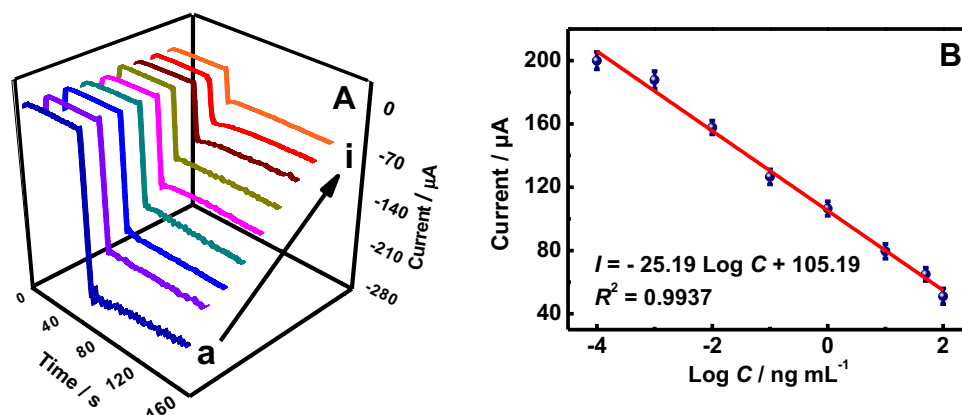


Table 1 Comparison of the as-developed sensor with those previously reported for the assay of PCT

Method	Materials	Linear range (ng mL ⁻¹)	LOD (pg mL ⁻¹)	Ref
CL	Biotin streptavidin-mediated peroxidase nanocomplex	0.0025 ~ 80	0.5	[8]
Colorimetry	MgFe ₂ O ₄ @Cys	0.0001 ~ 50	0.0449	[9]
EC	g-C ₃ N ₄ -NiCo ₂ S ₄ -CNTs-Ag NPs	0.001 ~ 10	0.33	[10]
PEC	Au NPs/BiOI NSs/B-TiO ₂ NPs, PbS/Co ₃ O ₄	0.0001 ~ 50	0.02	[49]
SIE	—	0.125 ~ 128	81	[55]
CL	PTC-DEPA/KCC-1 NCs, Au@Ag NPs	0.00005 ~ 10	0.017	[56]
EC	AuPtCu NDs/G-Co@ NCNBs	0.0001 ~ 100	0.011	This work

CL chemiluminescence, EC electrochemistry, PEC photoelectrochemistry, SIE Sandwich imaging ellipsometry, MgFe₂O₄@Cys MgFe₂O₄ modified with cysteine, g-C₃N₄ graphite carbon nitride, CNTs carbon nanotubes, Ag NPs argentum nanoparticles, Au NPs/BiOI NSs/B-TiO₂ NPs Au nanoparticles/BiOI nanosheets/Black TiO₂ nanoparticles, PbS/Co₃O₄ PbS quantum dots/Co₃O₄ polyhedron, PTC-DEPA/KCC-1 NCs perylene-3,4,9,10-tetracarboxylic acid-N,N-Diisopropylethylenediamine/mesoporous fibrous silica nanocomposites, Au@Ag NPs Au@Ag nanoparticles, AuPtCu NDs AuPtCu nanodendrites, G-Co@ NCNBs graphene-wrapped Co nanoparticle encapsulated in 3D N-doped carbon nanobrushes

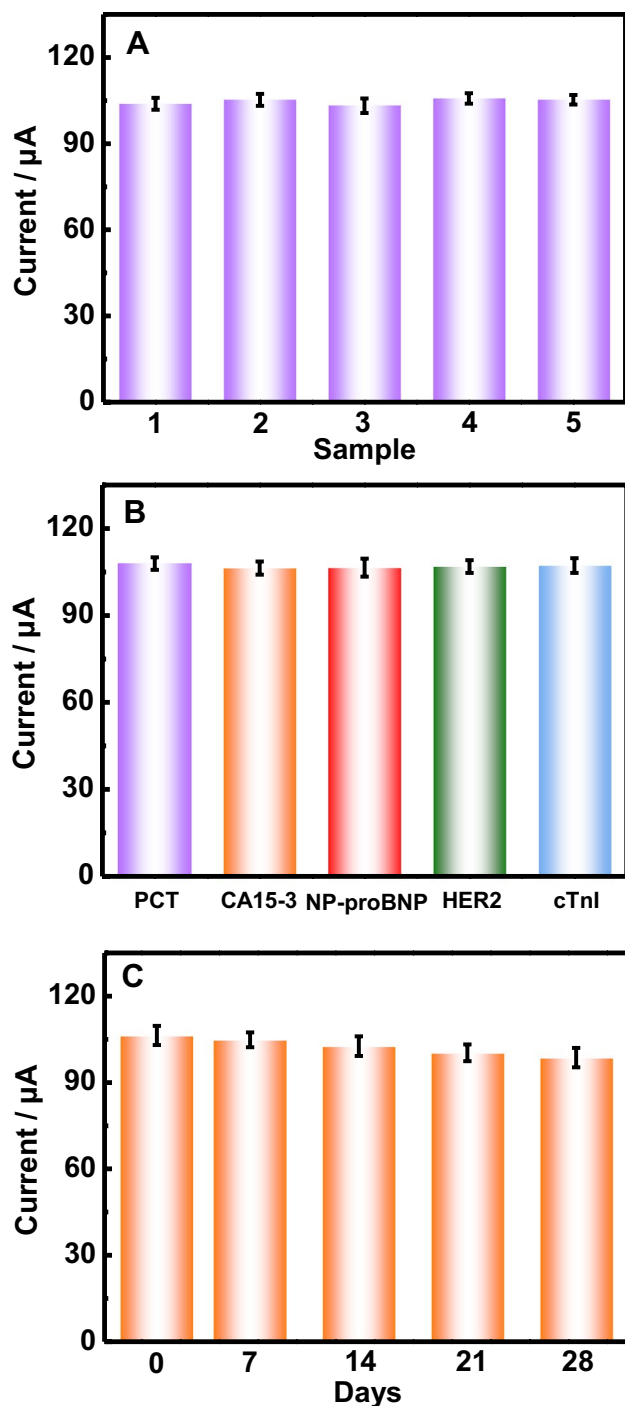


Fig. 9 (A) Electrochemical responses of the five sensors fabricated independently at 1.0 ng mL^{-1} PCT. (B) The currents acquired at 1.0 ng mL^{-1} PCT without and with 100.0 ng mL^{-1} CA15-3, NP-proBNP, HER2, and cTnI. (C) The storage stability examined at 1.0 ng mL^{-1} PCT (Error bar=SD, $n=5$). All of the tests were conducted in the PBS containing $5.0 \text{ mmol L}^{-1} \text{ H}_2\text{O}_2$

at 1.0 ng mL^{-1} PCT (Fig. 9A). Importantly, the relative standard deviation (RSD) of the acquired signals is lower than 2.47%, indicating the superior reproducibility.

The specificity is another significant index in the application of such sensors [14, 58]. Specificity test was conducted by blending 1.0 ng mL^{-1} PCT with 50 ng mL^{-1} other different tumor markers, such as carbohydrate antigen 15-3 (CA 15-3), N-terminal pro-B-type natriuretic peptide (NT-proBNP), human epidermal growth factor receptor 2 (HER2), and cardiac troponin I (cTnI). As Fig. 9B illustrates, the variations in the signals fluctuate within 1.45% relative to pure PCT, showing the satisfactory specificity of the as-prepared sensor for assaying PCT.

The stability of immunosensors shows close correlation with the practical applications [23]. For such a test, a series of the sensors were fabricated independently and stored at $4 \text{ }^\circ\text{C}$ for 28 days. The electrochemical signals decreased by 7.22% in this test, showing the acceptable stability (Fig. 9C).

Analysis of the serum sample

To evaluate the applicability of the as-developed sensor in a complicated real sample, we analyzed the PCT content in the human serum sample (initially diluted the received sample with the tenfold PBS) and performed the spike and recovery experiments by a standard addition method. After addition of 1.0 ng mL^{-1} and 10.0 ng mL^{-1} PCT to the diluted serum samples, the recovery values of the as-built sensor show up in a scope of 99.00~100.30% with the RSD below 2.99% (Table S1, SI). The analytical data certify feasibility of the biosensor for analysis of PCT in real samples.

To sum up, the follow-up aspects account for the appealing performance of the biosensor: (1) the dendritic structure of the AuPtCu NDs and hierarchical brushes of the G-Co@NCNBs create abundant active sites readily accessible, which significantly promote the interfacial electron transfer. (2) The unique structural features also enlarge the loading capacity of the immobilized biomolecules and magnify the detection signals. (3) The structural characteristics and synergistic impacts among the AuPtCu NDs and G-Co@NCNBs facilitate the electron transport between diverse electroactive substances and improved the catalytic property towards the H_2O_2 reduction, coupled by enhancing the conductivity and stability. Nevertheless, the method suffers from the longer incubation time (50 min), combined by disposable usage for the detection due to irreversibility of the highly specific immune-reaction. To this end, it is urgent for developing low-cost and disposable immunosensors for the commercial applications in the future.

Conclusions

In general, 3D G-Co@NCNBs and AuPtCu NDs were fabricated by the self-catalyzed chemical vapor deposition and one-pot solvothermal method, respectively. A novel

immunosensing platform for the quantitative bioassay of PCT was constructed using G-Co@NCNBs and AuPtCu NDs. Their coexistence displayed synergistic effects on the enhanced catalytic habits towards H_2O_2 reduction, which successfully acted as the prominent signal amplifier for immunosensing and created plenty of binding sites for the immune reaction upon immobilization of the Ab. Moreover, the resultant sensor showed a wide linear range ($0.0001 \sim 100 \text{ ng mL}^{-1}$) and a LOD down to 0.011 pg mL^{-1} ($S/N=3$). Also, this sensor displayed good reproducibility, excellent sensitivity, and acceptable stability coupled by exploring the analysis of PCT in real serum samples with the acceptable recovery rate. This method demonstrates the synergistic effects between noble metal materials and carbon nanomaterials, which provide some instructive insights in the construction of advanced biosensors in bioanalysis and clinical detection.

Supplementary Information The online version contains supplementary material available at <https://doi.org/10.1007/s00604-022-05179-8>.

Funding This research was supported by the Natural Science Foundation of Zhejiang Province (LQ20B050001), Zhejiang Public Welfare Technology Application Research Project (LGG19B050001), and National Students' Innovation and Entrepreneurship Training Program of Zhejiang Normal University (202110345022 for X.Y. Ge).

Declarations

Conflict of interest The authors declare no competing interests.

References

- Guo SY, Zhou Y, Hu QF, Yao J, Wang H (2015) Procalcitonin is a marker of gram-negative bacteremia in patients with sepsis. *Am J Med Sci* 349:499–504
- Molinero Fernández Á, Moreno Guzmán M, Arruza L, López MÁ, Escarpa A (2019) Toward early diagnosis of late-onset sepsis in preterm neonates: dual magnetoimmunosensor for simultaneous procalcitonin and c-reactive protein determination in diagnosed clinical samples. *ACS Sens* 4:2117–2123
- Herrera A, Vu BG, Stach CS, Merriman JA, Horswill AR, Salgado Pabón W, Schlievert PM (2016) *Staphylococcus aureus* β -toxin mutants are defective in biofilm ligase and sphingomyelinase activity, and causation of infective endocarditis and sepsis. *Biochemistry* 55:2510–2517
- Molinero Fernández Á, Moreno Guzmán M, Arruza L, López MÁ, Escarpa A (2020) Polymer-based micromotor fluorescence immunoassay for on-the-move sensitive procalcitonin determination in very low birth weight infants' plasma. *ACS Sens* 5:1336–1344
- Reyes Mondragón AL, Cantú-Rodríguez OG, Garza-Acosta AC, Gutiérrez-Aguirre CH, Colunga Pedraza PR, del Carmen Tarín-Arzaga L, Jaime-Pérez JC, Hawing Zárate JA, González-Cantú GA, Villalobos-Gutiérrez LE, Jiménez-Castillo RA, Vera-Pineda R, Gómez-Almaguer D (2021) Performance of serum procalcitonin as a biochemical predictor of death in hematology patients with febrile neutropenia. *Blood Cells Mol Dis* 90:102586
- Halder R, Seth T, Chaturvedi PK, Mishra P, Mahapatra M, Pati HP, Tyagi S, Saxena R (2020) Comparison of CRP and procalcitonin for etiological diagnosis of fever during febrile neutropenia in hematology patients—an experience from a tertiary care center in Northern India. *Blood Cells Mol Dis* 84:102445
- Shen WJ, Zhuo Y, Chai YQ, Yang ZH, Han J, Yuan R (2015) Enzyme-free electrochemical immunosensor based on host–guest nanonets catalyzing amplification for procalcitonin detection. *ACS Appl Mater Interfaces* 7:4127–4134
- Nie RB, Xu XX, Cui XJ, Chen YP, Yang L (2019) A highly sensitive capillary-based immunosensor by combining with peroxidase nanocomplex-mediated signal amplification for detection of procalcitonin in human serum. *ACS Omega* 4:6210–6217
- Li YY, Liu L, Wang YG, Ren R, Fan DW, Wu D, Du Y, Xu K, Ren X, Wei Q (2020) Enzyme-free colorimetric immunoassay for procalcitonin based on $MgFe_2O_4$ sacrificial probe with the Prussian blue production. *Sens Actuators B Chem* 316:128163
- Xu XT, Li X, Miao JC, Liu L, Huang XY, Wei Q, Cao W (2021) A dual-mode label-free electrochemical immunosensor for ultrasensitive detection of procalcitonin based on g- C_3N_4 - $NiCo_2S_4$ -CNTs-Ag NPs. *Analyst* 146:3169–3176
- Sun DF, Li HJ, Li MJ, Li CP, Qian LR, Yang BH (2019) Electrochemical immunosensors with AuPt-vertical graphene/glassy carbon electrode for alpha-fetoprotein detection based on label-free and sandwich-type strategies. *Biosens Bioelectron* 132:68–75
- Ding H, Yang L, Jia HY, Fan DW, Zhang Y, Sun X, Wei Q, Ju HX (2020) Label-free electrochemical immunosensor with palladium nanoparticles functionalized $MoS_2/NiCo$ heterostructures for sensitive procalcitonin detection. *Sens Actuators B Chem* 312:127980
- Wang XY, Feng YG, Wang AJ, Mei LP, Luo XL, Xue YD, Feng JJ (2021) Facile construction of ratiometric electrochemical immunosensor using hierarchical PtCoIr nanowires and porous $SiO_2@Ag$ nanoparticles for accurate detection of septicemia biomarker. *Bioelectrochemistry* 140:107802
- Rizwan M, Elma S, Lim SA, Ahmed MU (2018) AuNPs/CNOs/SWCNTs/chitosan-nanocomposite modified electrochemical sensor for the label-free detection of carcinoembryonic antigen. *Biosens Bioelectron* 107:211–217
- Butmee P, Tumcharern G, Thouand G, Kalcher K, Samphao A (2020) An ultrasensitive immunosensor based on manganese dioxide-graphene nanoplatelets and core shell $Fe_3O_4@Au$ nanoparticles for label-free detection of carcinoembryonic antigen. *Bioelectrochemistry* 132:10
- Mahato K, Purohit B, Kumar A, Chandra P (2020) Clinically comparable impedimetric immunosensor for serum alkaline phosphatase detection based on electrochemically engineered Au-nano-dendroids and graphene oxide nanocomposite. *Biosens Bioelectron* 148:111815
- Cen SY, Feng YG, Zhu JH, Wang XY, Wang AJ, Luo XL, Feng JJ (2021) Eco-friendly one-pot aqueous synthesis of ultra-thin AuPdCu alloyed nanowire-like networks for highly sensitive immunoassay of creatine kinase-MB. *Sens Actuators B Chem* 333:129573
- Dong H, Cao LL, Tan ZL, Liu Q, Zhou J, Zhao PP, Wang P, Li YY, Ma WS, Dong YH (2020) A signal amplification strategy of CuPtRh CNB-embedded ammoniated Ti_3C_2 mxene for detecting cardiac troponin I by a sandwich-type electrochemical immunosensor. *ACS Appl Bio Mater* 3:377–384
- Yan Q, Cao LL, Dong H, Tan ZL, Liu Q, Zhang W, Zhao PP, Li YY, Liu YY, Dong YH (2019) Sensitive amperometric immunosensor with improved electrocatalytic Au@Pd urchin-shaped nanostructures for human epididymis specific protein 4 antigen detection. *Anal Chim Acta* 1069:117–125

20. Wu YW, Chen XL, Wang XF, Yang M, Xu FL, Hou CJ, Huo DQ (2021) A fluorescent biosensor based on prismatic hollow Metal-polydopamine frameworks and 6-carboxyfluorescein (FAM)-labeled protein aptamer for CA15-3 detection. *Sens Actuators B Chem* 329:129249
21. Sun B, Huang L, Su S, Luo S, Meng CF, Basit HMA, Xiao JK, Bian T, Su SC (2020) PtRhCu ternary alloy nanodendrites with enhanced catalytic activity and durability toward methanol electro-oxidation. *Mater Chem Phys* 252:123234
22. Yang QS, Wang P, Ma EH, Yu HX, Zhou KW, Tang CY, Ren J, Li YY, Liu Q, Dong YH (2021) A sandwich-type electrochemical immunosensor based on Au@Pd nanodendrite functionalized MoO₂ nanosheet for highly sensitive detection of HBsAg. *Bioelectrochemistry* 138:107713
23. Fan L, Yan YR, Guo B, Zhao M, Li J, Bian XT, Wu HP, Cheng W, Ding SJ (2019) Trimetallic hybrid nanodendrites and magnetic nanocomposites-based electrochemical immunosensor for ultrasensitive detection of serum human epididymis protein 4. *Sens Actuators B Chem* 296:126697
24. Li XJ, Du Y, Xu P, Li YY, Ren X, Ma HM, Wang H, Wei Q, Ju HX (2020) Signal-off electrochemiluminescence immunosensor based on Mn-Eumelanin coordination nanoparticles quenching PtCo-CuFe₂O₄-reduced graphene oxide enhanced luminol. *Sens Actuators B Chem* 323:128702
25. Fiorani A, Merino JP, Zanut A, Criado A, Valenti G, Prato M, Paolucci F (2019) Advanced carbon nanomaterials for electrochemiluminescent biosensor applications. *Curr Opin Electrochem* 16:66–74
26. Lan QC, Shen HF, Li J, Ren CL, Hu XY, Yang ZJ (2020) Facile synthesis of novel reduced graphene oxide@polystyrene nanospheres for sensitive label-free electrochemical immunoassay. *Chem Commun* 56:699–702
27. Luo H, Jiang WJ, Niu S, Zhang X, Zhang Y, Yuan LP, He CX, Hu JS (2020) Self-catalyzed growth of Co–N–C nanobrushes for efficient rechargeable Zn–air batteries. *Small* 16:2001171
28. Dong H, Cao LL, Zhao H, Liu SH, Liu Q, Wang P, Xu Z, Wang SJ, Li YY, Zhao PQ, Li YY (2020) “Gold-plated” IRMOF-3 and sea cucumber-like Pd@PtRh SNRs based sandwich-type immunosensor for dual-mode detection of PCT. *Biosens Bioelectron* 170:112667
29. Zhang AM, Guo WW, Ke H, Zhang X, Zhang H, Huang CS, Yang DP, Jia NQ, Cui DX (2018) Sandwich-format ECL immunosensor based on Au star@BSA-Luminol nanocomposites for determination of human chorionic gonadotropin. *Biosens Bioelectron* 101:219–226
30. Tran DT, Le HT, Hoa VH, Kim NH, Lee JH (2021) Dual-coupling ultrasmall iron-Ni₂P into P-doped porous carbon sheets assembled CuxS nanobrush arrays for overall water splitting. *Nano Energy* 84:105861
31. Meng HL, Lin SY, Feng JJ, Zhang L, Wang AJ (2022) Coordination regulated pyrolysis synthesis of ultrafine FeNi/(FeNi)₉S₈ nanoclusters/nitrogen, sulfur-codoped graphitic carbon nanosheets as efficient bifunctional oxygen electrocatalysts. *J Colloid Interface Sci* 610:573–582
32. Chen MT, Zhang RL, Feng JJ, Mei LP, Jiao Y, Zhang L, Wang AJ (2022) A facile one-pot room-temperature growth of self-supported ultrathin rhodium-iridium nanosheets as high-efficiency electrocatalysts for hydrogen evolution reaction. *J Colloid Interface Sci* 606:1707–1714
33. Ren WN, Zang WJ, Zhang HF, Bian JL, Chen ZF, Guan C, Cheng CW (2019) PtCo bimetallic nanoparticles encapsulated in N-doped carbon nanorod arrays for efficient electrocatalysis. *Carbon* 142:206–216
34. Lv YH, Li XW (2020) PtCo/N-doped carbon sheets derived from a simple pyrolysis of graphene oxide/ZIF-67/H₂PtCl₆ composites as an efficient catalyst for methanol electro-oxidation. *Int J Hydrogen Energy* 45:12766–12776
35. Wang T, Guo YR, Zhou ZX, Chang XH, Zheng J, Li XG (2016) Ni-Mo nanocatalysts on N-doped graphite nanotubes for highly efficient electrochemical hydrogen evolution in acid. *ACS Nano* 10:10397–10403
36. Wang Q, Zhang ZH, Shi SJ, Wu F, Zhang ZG, Li GN, Suo YG (2021) Highly active cobalt- and nitrogen-doped carbon derived from ZIF-67@melamine towards oxygen reduction reaction. *J Electroanal Chem* 894:115397
37. Chen S-Y, Yang J-S, Wu J-J (2018) Three-dimensional undoped crystalline SnO₂ nanodendrite arrays enable efficient charge separation in BiVO₄/SnO₂ heterojunction photoanodes for photoelectrochemical water splitting. *ACS Appl Energy Mater* 1:2143–2149
38. Gao YJ, Wang JM, Du YT, Wu CS, Li HX, Yang ZQ, Chen ZY, Yang ZJ (2021) N, O-codoped hierarchical porous graphitic carbon for electrochemical immunosensing of *Lactobacillus rhamnosus* GG. *Microchim Acta* 189:5
39. Sun RM, Zhang L, Feng JJ, Fang KM, Wang AJ (2022) In situ produced Co₉S₈ nanoclusters/Co/Mn-S, N multi-doped 3D porous carbon derived from eriochrome black T as an effective bifunctional oxygen electrocatalyst for rechargeable Zn-air batteries. *J Colloid Interface Sci* 608:2100–2110
40. Zhao ZL, Zhang LY, Bao SJ, Li CM (2015) One-pot synthesis of small and uniform Au@PtCu core–alloy shell nanoparticles as an efficient electrocatalyst for direct methanol fuel cells. *Appl Catal B* 174–175:361–366
41. Chen Y, Wang XY, Wang AJ, Mei LP, Yuan PX, Luo XL, Feng JJ (2021) Ultrasensitive ratiometric electrochemical immunoassay of N-terminal pro-B-type natriuretic peptide based on three-dimensional PtCoNi hollow multi-branches/ferrocene-grafted-ionic liquid and Co–N–C nanosheets. *Sens Actuators B Chem* 326:128794
42. Liu J, Cao L, Huang W, Li ZL (2011) Preparation of AuPt alloy foam films and their superior electrocatalytic activity for the oxidation of formic acid. *ACS Appl Mater Interfaces* 3:3552–3558
43. Zhang ZX, Xie M, Liu ZJ, Lu YM, Zhang SM, Liu MX, Liu K, Cheng T, Gao CB (2021) Ultrathin Pt–Cu–Ni ternary alloy nanowires with multimetallic interplay for boosted methanol oxidation activity. *ACS Appl Energy Mater* 4:6824–6832
44. Hu J, Wu L, Kuttiyiel KA, Goodman KR, Zhang C, Zhu Y, Vukmircovic MB, White MG, Sasaki K, Adzic RR (2016) Increasing stability and activity of core–shell catalysts by preferential segregation of oxide on edges and vertices: oxygen reduction on Ti–Au@Pt/C. *J Am Chem Soc* 138:9294–9300
45. Gnanaprakasam P, Gowrisankar A, Senthilkumar S, Murugadas A, Selvaraju T, Mangalaraja RV (2021) One pot in situ synthesis of nano Au–Pd core-shells embedded on reduced graphene oxide for the oxygen reduction reaction. *Mat Sci Eng B* 264:114924
46. Yadav N, Yadav RR, Dey KK (2022) Microwave assisted formation of trimetallic AuPtCu nanoparticles from bimetallic nanoclusters: why it is a superior new age biocidal agent compared to monometallic & bimetallic nanoparticles. *J Alloys Compd* 896:163073
47. Xu H, Yan B, Zhang K, Wang J, Li SM, Wang CQ, Xiong ZP, Shiraishi Y, Du YK, Yang P (2017) Sophisticated construction of hollow Au–Ag–Cu nanoflowers as highly efficient electrocatalysts toward ethylene glycol oxidation. *ACS Sustainable Chem Eng* 5:10490–10498
48. Liu YJ, Ren GH, Wang MQ, Zhang ZC, Liang Y, Wu SS, Shen J (2019) Facile synthesis of trimetallic PtAuCu alloy nanowires as high-performance electrocatalysts for methanol oxidation reaction. *J Alloys Compd* 780:504–511
49. Qian YR, Feng JH, Wang H, Fan DW, Jiang N, Wei Q, Ju HX (2019) Sandwich-type signal-off photoelectrochemical immunosensor based on dual suppression effect of PbS quantum dots/

- Co₃O₄ polyhedron as signal amplification for procalcitonin detection. *Sens Actuators B Chem* 300:127001
50. Li XC, He CJ, Zheng J, Wu DN, Duan YT, Li YF, Rao PH, Tang B, Rui YC (2020) Flocculent Cu caused by the jahn–teller effect improved the performance of Mg-MOF-74 as an anode material for lithium-ion batteries. *ACS Appl Mater Interfaces* 12:52864–52872
 51. Bhunia K, Khilari S, Pradhan D (2017) Trimetallic PtAuNi alloy nanoparticles as an efficient electrocatalyst for the methanol electrooxidation reaction. *Dalton Trans* 46:15558–15566
 52. Li ZJ, Jiang X, Wang XR, Hu JR, Liu YY, Fu GT, Tang YW (2020) Concave PtCo nanocrosses for methanol oxidation reaction. *Appl Catal B* 277:119135
 53. Zhang L, Zhang XF, Chen XL, Wang AJ, Han DM, Wang ZG, Feng JJ (2019) Facile solvothermal synthesis of Pt₇₁Co₂₉ lamellar nanoflowers as an efficient catalyst for oxygen reduction and methanol oxidation reactions. *J Colloid Interface Sci* 536:556–562
 54. Zhang XF, Meng HB, Chen HY, Feng JJ, Fang KM, Wang AJ (2019) Bimetallic PtCo alloyed nanodendritic assemblies as an advanced efficient and robust electrocatalyst for highly efficient hydrogen evolution and oxygen reduction. *J Alloys Compd* 786:232–239
 55. Li YK, Liu W, Jin G, Niu Y, Chen YP, Xie MX (2018) Label-free sandwich imaging ellipsometry immunosensor for serological detection of procalcitonin. *Anal Chem* 90:8002–8010
 56. Chen PP, Qiao XY, Liu JH, Xia FQ, Tian D, Zhou CL (2018) A dual-signals response electrochemiluminescence immunosensor based on PTC-DEPA/KCC-1 NCs for detection of procalcitonin. *Sens Actuators B Chem* 267:525–532
 57. Periyakaruppan A, Gandhiraman RP, Meyyappan M, Koehne JE (2013) Label-free detection of cardiac troponin-I using carbon nanofiber based nanoelectrode arrays. *Anal Chem* 85:3858–3863
 58. Lan QC, Ren CL, Lambert A, Zhang GS, Li J, Cheng Q, Hu XY, Yang ZJ (2020) Platinum nanoparticle-decorated graphene oxide@polystyrene nanospheres for label-free electrochemical immunosensing of tumor markers. *ACS Sustain Chem Eng* 8:4392–4399

Publisher's note Springer Nature remains neutral with regard to jurisdictional claims in published maps and institutional affiliations.